

ARTICLE

Open Access

# Nano calligraphy via optical electro-aligning manipulation

Haobing Liu<sup>1,2</sup>, Rongxin Fu<sup>3,4,5</sup>, Zongliang Guo<sup>6</sup>, Zonghao Li<sup>6</sup>, Menglei Zhao<sup>1,2</sup>, Ziyuan Li<sup>7,8</sup>, Dong Pan<sup>9</sup>, Yifan Zhang<sup>10</sup>, Chenyang Xi<sup>7,8</sup>, Hang Li<sup>3,4,5</sup>, Kangfu Chen<sup>4,5,6</sup>, Bing Chu<sup>11</sup>, Kai Lou<sup>11</sup>, Yanfeng Zhang<sup>12</sup>, Yujie Chen<sup>12</sup>, Huikai Xie<sup>4,5,6</sup>, Jiafang Li<sup>8</sup> and Shuailong Zhang<sup>2,4,5,6</sup>

## Abstract

The precision assembly of anisotropic nanostructures is a prerequisite for next-generation integrated microsystems, quantum photonics, and bio-interfaces. However, bridging the gap between individual manipulation accuracy and scalable, programmable manufacturing remains a grand challenge. Current optical and alternative physical field approaches are hindered by inadequate control stability, thermal damage, and interfacial adhesion limitations. Here, we report a robust hybrid opto-electric microsystem that synergizes alternating current (AC) electric fields with holographic optical tweezers to overcome these barriers. By introducing an Optical Electro-aligning Manipulation (OEM) strategy, we convert the stochastic motion of nanowires into deterministic, pre-aligned trajectories, significantly minimizing scattering forces and optimizing trapping stability. This results in a 38% increase in capture success rate, a 50% reduction in laser power requirements, and a 39% increase in translation speeds for Ag, TiO<sub>2</sub>, GaAs, and InAs nanowires. Furthermore, we demonstrate “nano-calligraphy” as a lithography-free patterning technique, enabling the programmable construction of complex micro-patterns with sub-micron resolution. The capability for parallel control of up to seven nanowires and the successful manipulation of biological agents (bacteria) confirm the system’s scalability and versatility. This work establishes a powerful nanomanufacturing platform for the bottom-up assembly of functional NEMS devices, photonic networks, and cellular nanoprobes.

## Introduction

Bottom-up assembly of one-dimensional nanostructures (e.g., nanowires, nanotubes) enables revolutionary advances in Nano-Electro-Mechanical Systems (NEMS), quantum devices, and biohybrid systems, owing to their anisotropic electronic and optical<sup>1</sup>. These anisotropic building blocks possess distinctive properties including plasmonic resonance<sup>2,3</sup>, quantum confinement<sup>4</sup>, and piezoelectric responses<sup>5</sup>, enabling breakthroughs in single-photon sources, neural probes, and ultrasensitive NEMS sensors. However, realizing the full potential of

these materials requires transforming laboratory-scale manipulation into reliable, scalable manufacturing processes capable of reconciling nanometer precision with high-throughput programmability.

State-of-the-art strategies for nanowire manipulation face fundamental engineering limitations<sup>6</sup>. Optical approaches, exemplified by optical tweezers (OT), offer non-contact control with sub-diffraction positioning accuracy<sup>7–9</sup>. However, for high-aspect-ratio nanostructures, which have elongated geometry and strong interactions with ambient environments, OT manipulation faces significant challenges. Improved methods include light field modulation strategies that optimize light-matter interactions. For instance, photonic nanojets have been utilized to regulate soft microalga-robots for controllable navigation<sup>10</sup>. Similarly, by tailoring light fields with advanced photonic structures<sup>11,12</sup>, plasmonic hybridization, where metallic nanostructures generate

Correspondence: Rongxin Fu (furongxin@bit.edu.cn) or Shuailong Zhang (shuailong.zhang@bit.edu.cn)

<sup>1</sup>School of Mechatronics Engineering, Beijing Institute of Technology, Beijing, China

<sup>2</sup>Zhengzhou Research Institute, Beijing Institute of Technology, Zhengzhou, China

Full list of author information is available at the end of the article

© The Author(s) 2026



**Open Access** This article is licensed under a Creative Commons Attribution-NonCommercial-NoDerivatives 4.0 International License, which permits any non-commercial use, sharing, distribution and reproduction in any medium or format, as long as you give appropriate credit to the original author(s) and the source, provide a link to the Creative Commons licence, and indicate if you modified the licensed material. You do not have permission under this licence to share adapted material derived from this article or parts of it. The images or other third party material in this article are included in the article's Creative Commons licence, unless indicated otherwise in a credit line to the material. If material is not included in the article's Creative Commons licence and your intended use is not permitted by statutory regulation or exceeds the permitted use, you will need to obtain permission directly from the copyright holder. To view a copy of this licence, visit <http://creativecommons.org/licenses/by-nc-nd/4.0/>.

localized surface plasmon resonances to confine light at subwavelength scales, enables high-precision trapping of nanoparticles with reduced laser power<sup>13</sup>. Another method involves customizing the shape of light fields, tailoring the spatial profile of the laser beam to enhance 3D trap stiffness without increasing laser power<sup>14</sup>. Despite progress, localized heating, the lack of anisotropic optical response modeling and insufficient orientation/stiffness control for nanowire manipulation remain bottlenecks. Alternative physical-field methods, for example, opto-thermoelectric nanotweezers and recent highly adaptable optothermal traps<sup>15,16</sup>, combine laser-induced thermal gradients and alternating current (AC) electric fields to generate electro-thermo-plasmonic flows or manage solid-liquid interfaces for molecular sensing<sup>17</sup>; optoelectronic tweezers (OET) apply a nonuniform electric field to dynamically manipulate and separate individual semiconducting and metallic nanowires<sup>18</sup>. Constrained by limitations in three-dimensional manipulation and substrate adhesion, these methods fail to deliver the precision, versatility, and biocompatibility required by next-generation applications<sup>19–21</sup>.

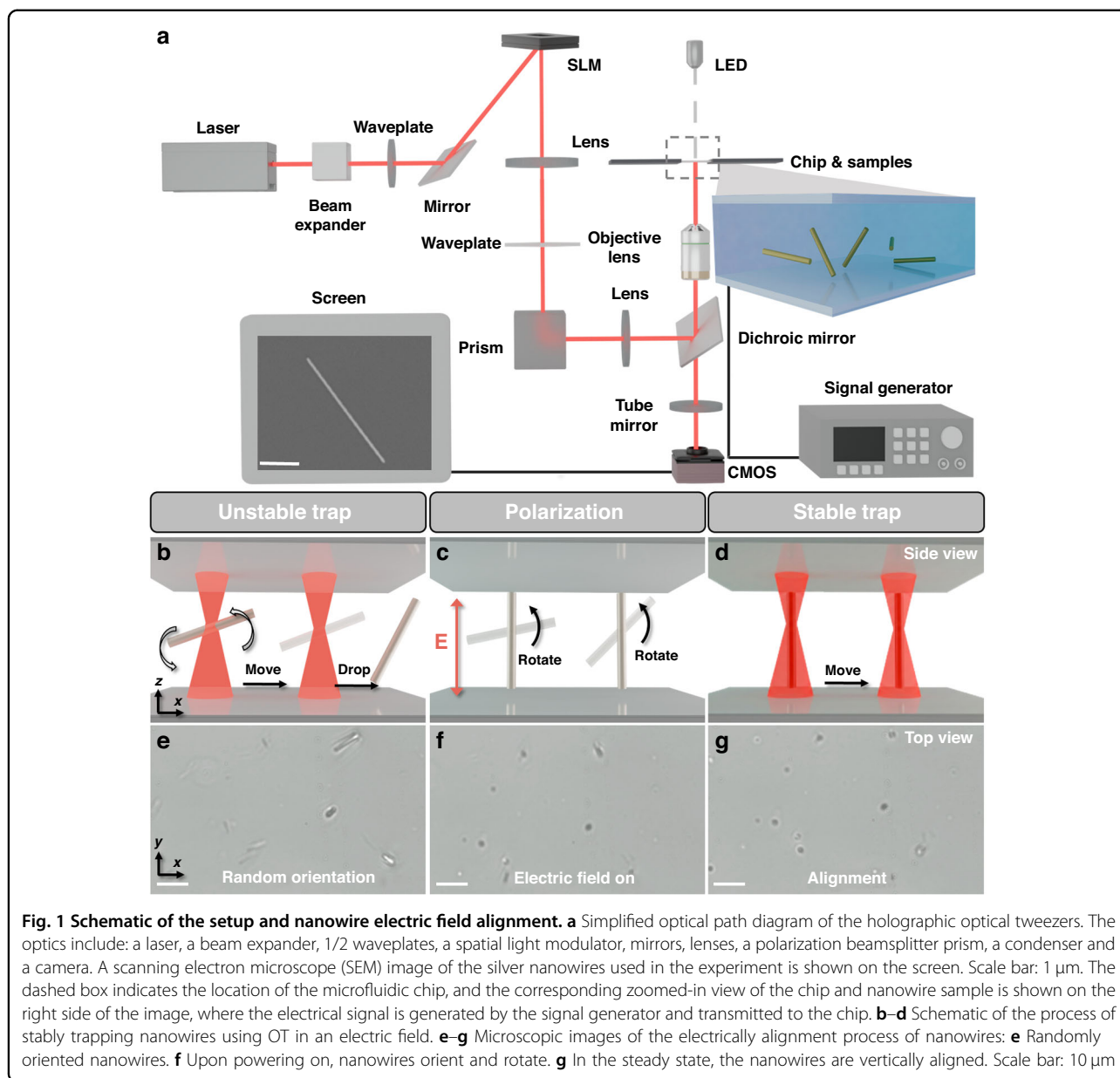
Herein, we propose and demonstrate an Optical Electro-aligning Manipulation (OEM) strategy to address the challenge of nanowire manipulation. This technique integrates a holographic OT system with a spatially uniform AC electric field. Our strategy leverages the synergy of two physical fields (Fig. 1): (1) the AC field provides a deterministic alignment torque to pre-orient nanowires, suppressing orientational entropy; (2) the OT provides high-precision spatial positioning. By engineering this field coupling, we maximize the polarizability anisotropy of the nanowires, amplifying gradient forces while minimizing scattering. We employ finite element simulations combined with theoretical models to qualitatively explain these two physical phenomena (Fig. 2). We experimentally validated the OEM strategy on various metal and semiconductor nanowires using a custom-fabricated OT chip designed to integrate the AC electric field. Consequently, the success rate for optically trapping pre-aligned nanowires increased by 38% compared to that of conventional OT. Furthermore, the OEM approach reduced the optical power threshold for stable trapping by 50% and increased the maximum manipulation speed by 39% (Fig. 3). To highlight the manufacturing capabilities of our platform, we demonstrate intricate nano-calligraphy by using nanowires as optically guided brushes, showcasing precise, programmable manipulation of both single and multiple nanowires in parallel (Fig. 4). The versatility of the OEM strategy was further confirmed by extending its application to other rod-shaped nanostructures, such as *Bacillus subtilis* bacteria (Fig. 5). This hybrid opto-electric framework establishes a powerful and versatile platform for multi-modal micro- and nanomanipulation,

contributing to the fundamental understanding and application of hybrid-field control over matter.

## Results

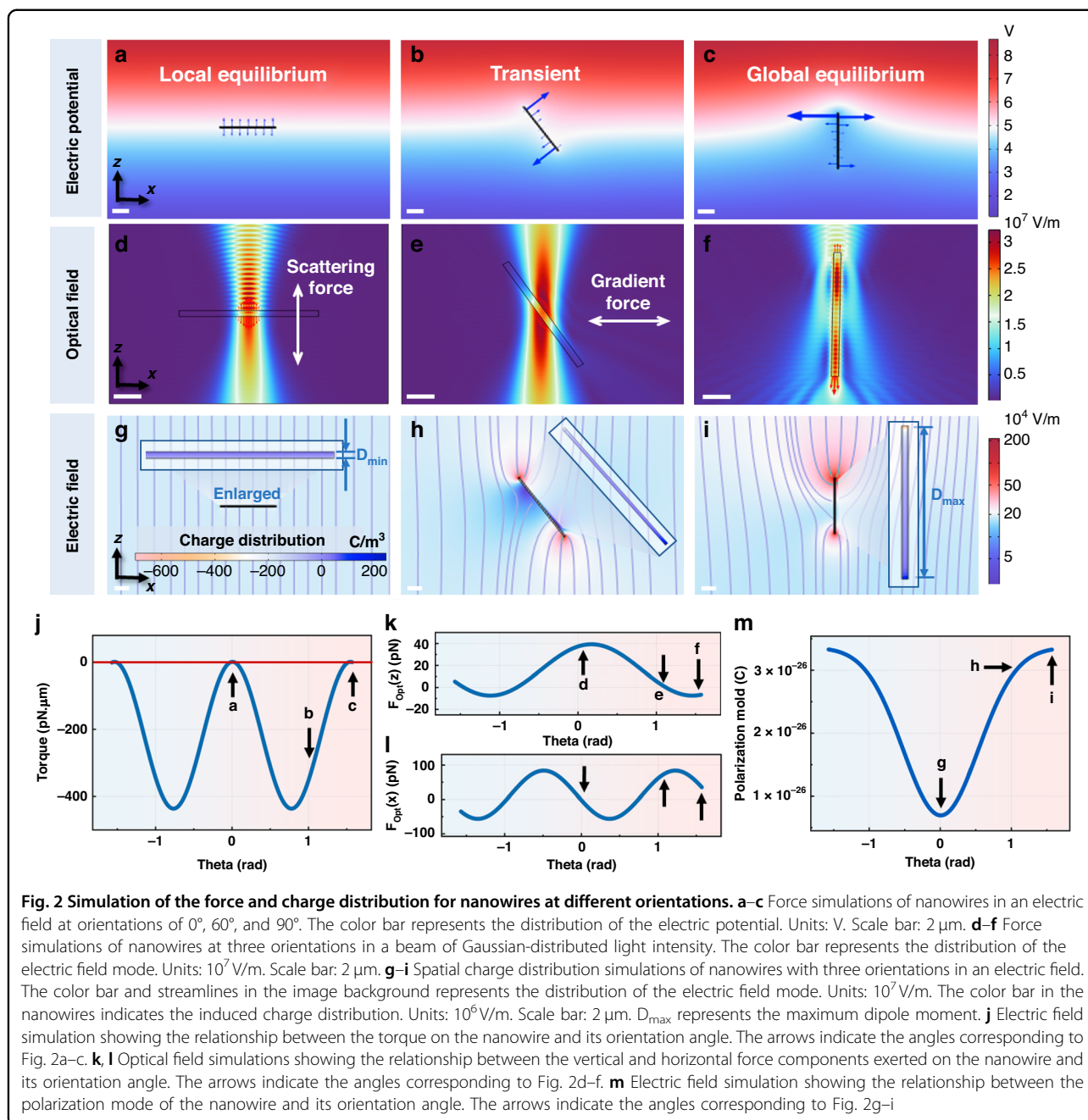
Figure 1 illustrates the schematic of the experimental setup and the fundamental principle of the OEM strategy. Our apparatus is a multiphysics-coupled system that integrates a holographic OT with an electrical control module. A photograph of the physical apparatus is provided in the Fig. S1. Figure 1a shows a simplified optical path diagram. The 1064-nm laser reaches the back aperture of the objective after expansion and modulation by a series of mirrors, lenses, and a spatial light modulator. To generate a sufficiently strong optical gradient force, a 100× oil immersion objective with a numerical aperture of 1.3 was used. The zoomed-in schematic (indicated by the dashed box) details the custom-designed OT chip, which features a three-layer sandwich structure. A liquid suspension of nanowires is sealed between two transparent indium tin oxide (ITO)-coated glass slides that serve as electrodes. An AC signal, produced by a function generator and subsequently amplified, is applied to these ITO electrodes to generate a uniform electric field within the sample chamber. Detailed information please see in Methods Section. Real-time imaging of the manipulation is performed using a CMOS camera. A representative SEM image of a silver nanowire (3 μm in length, 100 nm in diameter) is also shown. As illustrated in Fig. 1b, conventional optical trapping of nanowires is inherently challenging. Their high aspect ratio results in a dominant optical scattering force, which typically prevents the stable trapping of randomly oriented nanowires. However, we observe that applying an AC electric field induces a rapid reorientation of both metal and semiconductor nanowires. This reorientation arises from the torque exerted by the electric field on the induced dipole moment of the nanowire. This process, termed electric alignment or polarization, is depicted in Fig. 1c. Once aligned, the nanowires can be stably trapped and manipulated by the OT (Fig. 1d), a consequence of the enhanced gradient force and minimized optical scattering. Figure 1e–g provide a temporal sequence of microscope images documenting this electric alignment process. Initially, the nanowires are randomly oriented (Fig. 1e). Upon application of the AC field, they promptly rotate to align with the field lines (Fig. 1f). Finally, they become stably aligned with their long axis perpendicular to the imaging plane, such that only their cross-section is visible (Fig. 1g). A video demonstrating the dynamics of this alignment process is available in the Movie S1.

To elucidate the electric and optical forces acting on the nanowires, we performed finite element method simulations. The simulations modeled a silver nanowire (10 μm



in length, 200 nm in diameter) suspended in a rectangular aqueous domain ( $100 \mu\text{m} \times 40 \mu\text{m}$ ), as shown in Fig. S2. An AC potential difference of 10 V was applied across the z-direction of the domain to generate the electric field. Further simulation parameters are detailed in the Supplementary Information. To theoretically elucidate the alignment mechanism, we initially employed a simplified 2D model in the x-z plane to visualize the resultant forces. We acknowledge that this 2D model approximates the nanowire geometry as an infinite plate rather than a finite cylinder. To rigorously validate the physical mechanism, we further performed full 3D finite element simulations (see Figs. S3–5 in Supplementary Information). The 3D results exhibit excellent qualitative agreement with the 2D

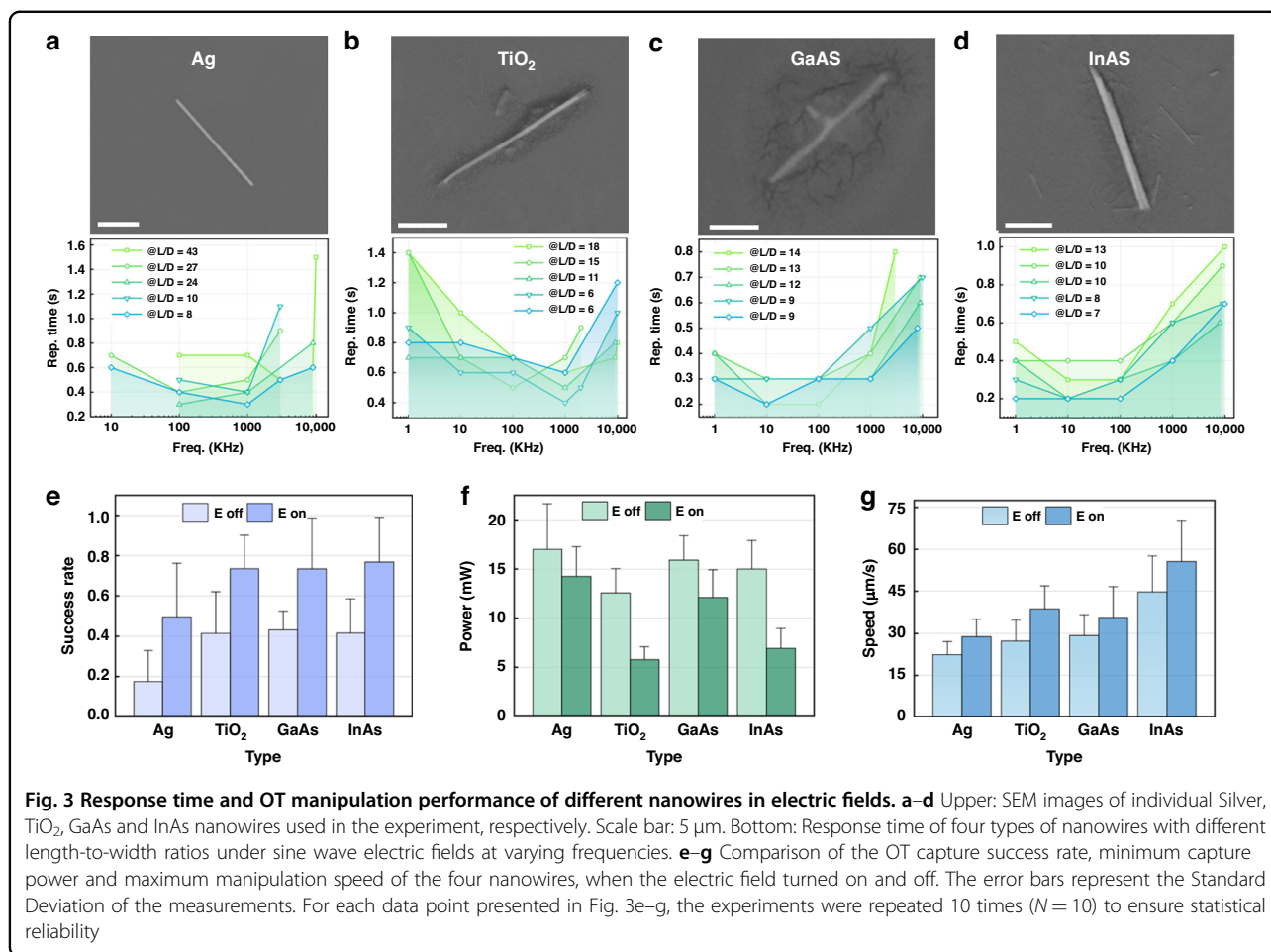
analysis, confirming that the charge concentration at the nanowire tips generates a restorative torque that drives the nanowire toward a stable vertical equilibrium. To elucidate the interaction between the optical and electric fields, we considered the vast frequency disparity between the AC electric field and the optical trapping laser. Theoretically, this time-scale separation implies that direct electromagnetic interference is negligible. To rigorously validate this, we performed a verification using a fully coupled multi-physics model, shown in Fig. S6. The results confirmed that the influence of the low-frequency electric polarization on the optical field propagation is minimal. The nanowire was rotated by 1 degree with a fixed step size, starting from a position parallel to the X-



axis, and rotated through 180 degrees while recording the electric field force at each orientation. Figure 2a–c depicts the results for three representative angles:  $0^\circ$ ,  $60^\circ$ , and  $90^\circ$ . In these panels, the color map represents the electric potential distribution, while the blue arrows indicate the direction and relative magnitude of the resultant electric force.

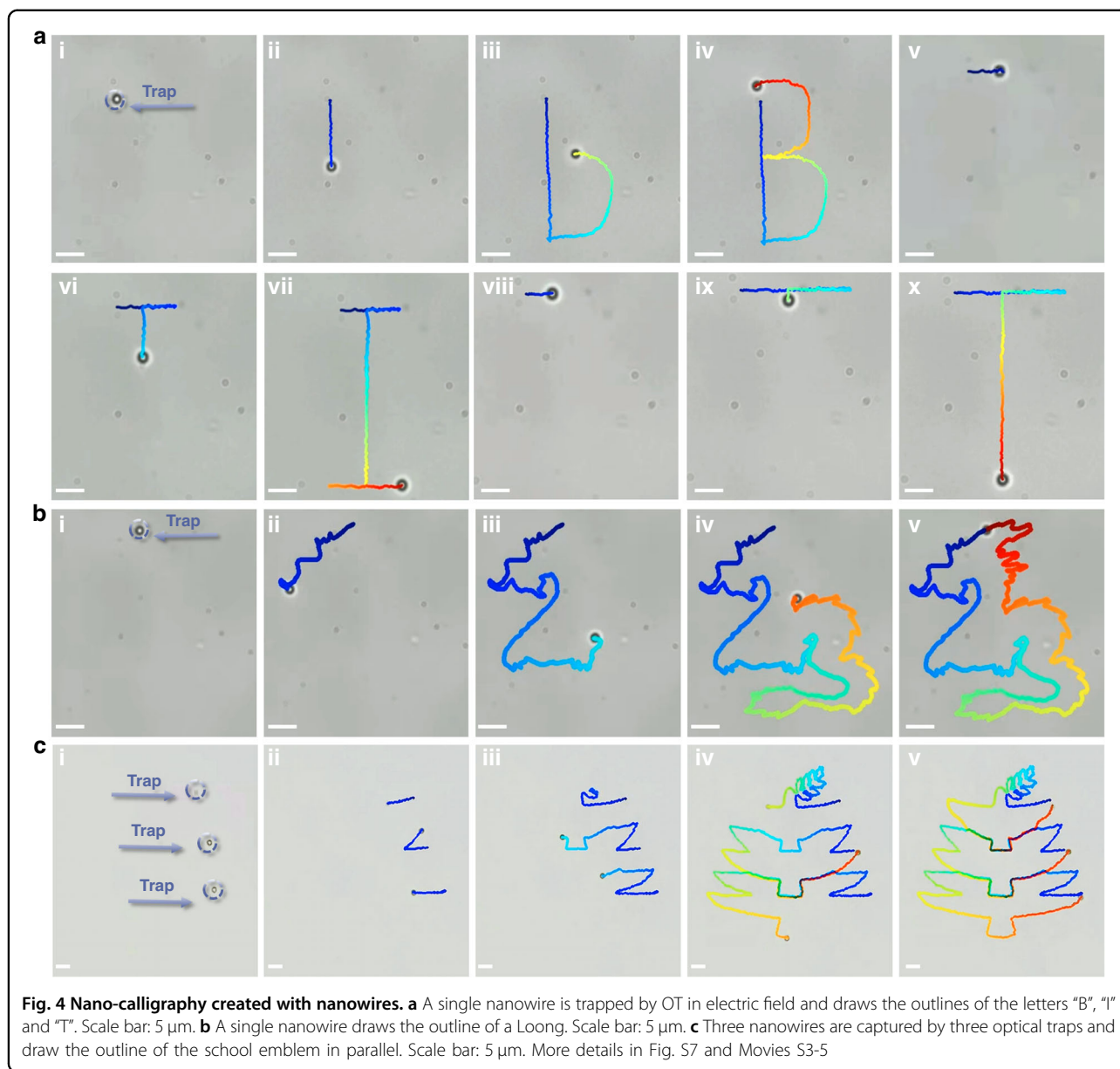
At  $0^\circ$  (Fig. 2a), where the nanowire is perpendicular to the electric field, it experiences a symmetric and relatively weak net force. However, this orientation represents an unstable equilibrium; any minor perturbation creates a

net torque that induces rotation. Figure 2b shows a transient state at  $60^\circ$ , where this induced torque is actively reorienting the nanowire. At  $90^\circ$  (Fig. 2c), the nanowire aligns parallel to the electric field, reaching a stable equilibrium where both the net force and torque are minimized. Next, we simulated the optical forces exerted on the same nanowire model by a focused Gaussian beam, characteristic of an optical tweezer. In this 2D model, the axial force along the z-axis, the direction of beam propagation, is dominated by the scattering force, while the transverse force along the x-axis is primarily the gradient



force. When the nanowire is oriented perpendicular to the beam axis (Fig. 2d), it experiences a strong axial scattering force, pushing it out of the trap. At an oblique angle (Fig. 2e), the nanowire is subjected to a complex combination of forces and torques that are typically unbalanced, leading to unstable dynamics. Conversely, when the nanowire is aligned parallel to the beam's propagation direction (Fig. 2f), the scattering forces are minimized and balanced, allowing the transverse gradient force to stably confine the nanowire at the beam's focus. In addition, we simulated the induced charge distribution and resulting dipole moment of the nanowire within the electric field in Fig. 2g–i. In these figures, the background shows the electric field streamlines and intensity distribution. When the nanowire is perpendicular to the electric field (Fig. 2g), the charge separation is negligible, resulting in a minimal induced dipole moment. As the nanowire rotates to align with the field, charge accumulates at its ends, and the induced dipole moment increases, reaching its maximum when fully aligned (Fig. 2i). Movie S2 shows the dynamic evolution of the charge distribution and dipole moment during this rotation.

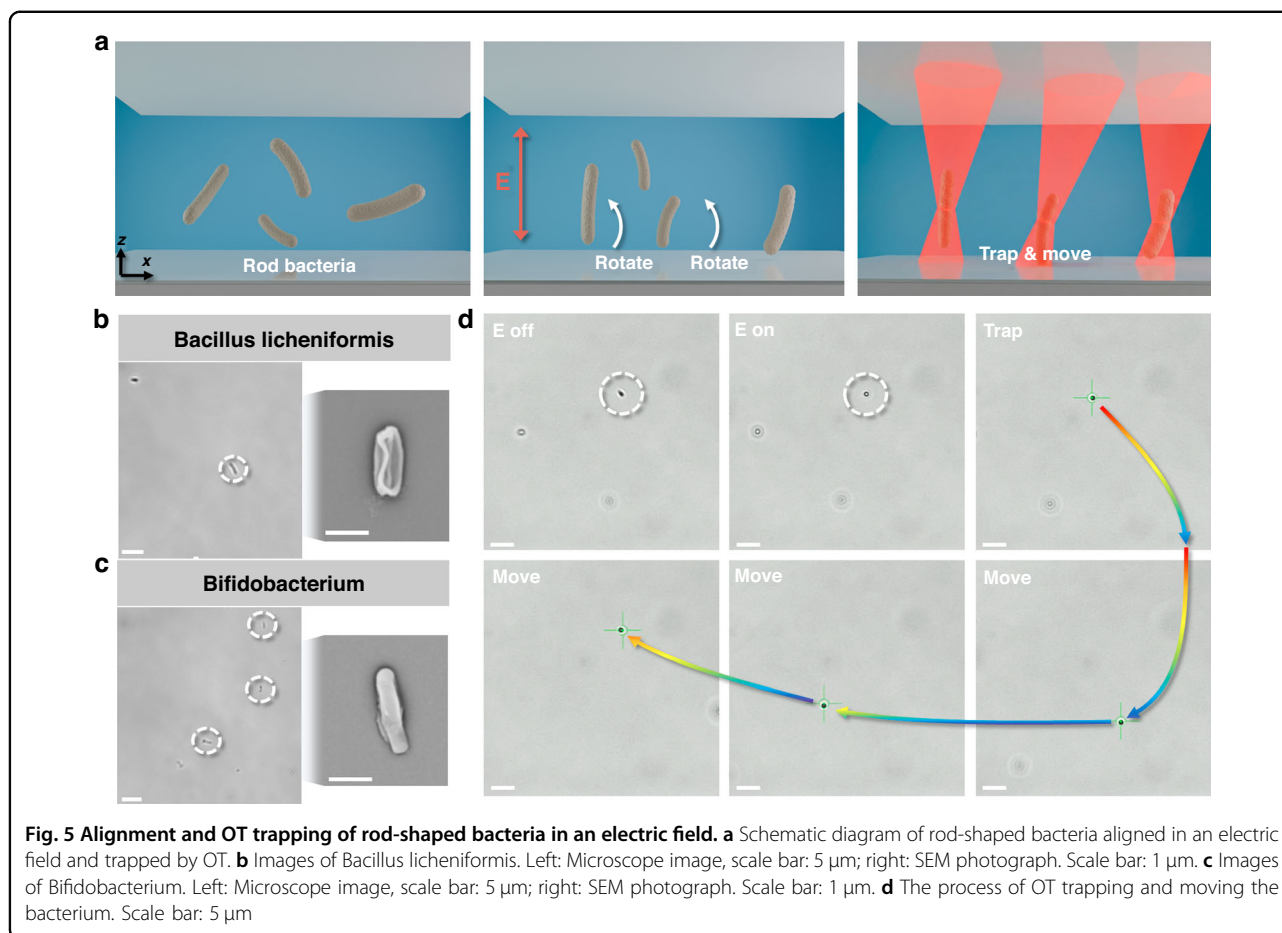
Figure 2j–m provide a quantitative analysis of the simulation results, corresponding to the orientations depicted in Fig. 2a–i. Figure 2j plots the calculated electric-field-induced torque on the nanowire as a function of its orientation angle. The torque is zero at 0° and 90°, corresponding to the unstable (Fig. 2a) and stable (Fig. 2c) equilibrium positions, respectively. At intermediate angles, a significant restoring torque, reaching a maximum magnitude of approximately 400 pN  $\mu\text{m}$ , acts to drive the nanowire toward the stable, field-aligned orientation. The calculated optical forces are decomposed into their axial (scattering) and transverse (gradient) components in Fig. 2k, l, respectively. The axial scattering force, which acts to destabilize the trap, is maximized at  $\approx 40$  pN when the nanowire is perpendicular to the beam axis (0°, Fig. 2d) and is minimized ( $<1$  pN) in the parallel orientation (90°, Fig. 2f). Conversely, the transverse gradient force, which provides confinement, is strongest at intermediate angles and diminishes as the nanowire approaches either a fully perpendicular or parallel orientation. Finally, Fig. 2m quantifies the magnitude of the induced dipole moment as a function of angle. The dipole



moment is minimal when the nanowire is perpendicular to the electric field ( $0^\circ$ ) and maximal when parallel to it ( $90^\circ$ ), with the two states differing by nearly an order of magnitude.

To validate the OEM strategy and quantify its performance benefits, we conducted experiments on four distinct metal and semiconductor nanowires: silver (Ag), titanium dioxide ( $\text{TiO}_2$ ), gallium arsenide (GaAs), and indium arsenide (InAs), all possessing an average aspect ratio exceeding 10. Representative SEM images of individual nanowires for each material are presented in the upper panels of Fig. 3a–d. The Ag and  $\text{TiO}_2$  nanowires were commercially sourced, whereas the GaAs and InAs nanowires were synthesized in-house. Synthesis and

material details are provided in the Methods and Supplementary Information. Morphologically, the Ag nanowires exhibit superior size uniformity, whereas the  $\text{TiO}_2$  nanowires possess a larger average length and diameter. To characterize the electrokinetic behavior of each material, we first measured the alignment response time of the nanowires to the applied AC electric field. The response time was defined as the interval from field application to the moment the nanowire’s major axis first became parallel with the electric field lines, determined via frame-by-frame video analysis. This method provides temporal resolution in the millisecond range. Fundamentally, this alignment is a passive process driven by the torque generated from the interaction between the field



and the nanowire's induced dipole moment<sup>22</sup>. The magnitude of this torque is proportional to the real part of the Clausius–Mossotti (CM) factor, a frequency-dependent term related to the dielectric properties of the nanowire and the surrounding medium. Our experimental conclusions are consistent with previous studies<sup>23–27</sup> which show that Ag nanowires respond fastest at higher frequencies ( $\geq 1$  MHz), with alignment times of 0.1–1 s. In contrast, the semiconductor nanowires (GaAs, InAs) exhibit optimal alignment in the mid-frequency range (500 kHz–5 MHz)<sup>28–32</sup>, with response times of 0.2–0.8 s. We also observed that for a given material, nanowires with larger aspect ratios generally exhibited longer alignment times (Fig. 3a–d), consistent with an increase in rotational drag. However, this geometric factor also plays a constructive role: a larger aspect ratio significantly enhances the nanowire's polarizability anisotropy (as detailed in Supplementary Information). This anisotropy is the origin of the alignment torque itself. Therefore, a high-aspect-ratio geometry, while increasing drag, is also fundamental to generating the strong, stable alignment torque that underpins the high trapping success rates and enhanced manipulation speeds observed in Fig. 3e–g.

Following the electrical characterization, we quantitatively evaluated the enhancement in optical trapping performance afforded by the OEM strategy. As shown in Fig. 3e, applying the AC field dramatically improved the trapping success rate (The mathematical definition is in Methods part) for all four nanowire types, increasing from a baseline of approximately 40% with conventional OT to as high as 78% with the OEM technique. Furthermore, the optical power threshold for stable trapping was reduced by up to 50%, decreasing from a mean of 15 mW to 7 mW (Fig. 3f). The maximum manipulation speed before nanowire escape from the trap also increased significantly, by up to 39% (from 26  $\mu\text{m}/\text{s}$  to 36  $\mu\text{m}/\text{s}$ ), as shown in Fig. 3g. Taken together, these results provide compelling evidence that the OEM strategy substantially enhances the performance and robustness of optical manipulation for high-aspect-ratio nanostructures.

To showcase the high degree of stability and programmable control afforded by the OEM strategy, we utilized optically trapped nanowires as styluses to trace pre-defined calligraphic patterns. As established, the vertically aligned nanowires present only their circular cross-section to the top-down imaging plane, appearing as

distinct points of contrast in the micrograph. The apparent diameter of these points (typically a few hundred nanometers to one micrometer) is a result of diffraction and scattering from the nanowire tip. In a demonstration of single-nanowire control, we trapped an individual nanowire and translated it along a programmed trajectory to trace the letters “BIT” at a constant speed of 15  $\mu\text{m/s}$  (Fig. 4a). The entire process is shown in Movie S3. To demonstrate the tracing of more intricate paths, another nanowire was guided at a lower speed to outline the complex form of a Loong (The Chinese Dragon, a legendary creature in Chinese mythology), as shown in Fig. 4b. Throughout these manipulations, the nanowire remained stably confined within the optical trap, exhibiting only minimal Brownian motion. Movie S4 records the entire process. A key advantage of the integrated holographic OT system is the capacity for parallel manipulation of multiple nanowires. As depicted in Fig. 4c, we simultaneously trapped three individual nanowires in independent optical traps and coordinated their movement to trace the outline of the Beijing Institute of Technology (BIT) emblem. In these parallel manipulations, we achieved a minimum center-to-center separation of approximately 2  $\mu\text{m}$  between adjacent nanowires. Notably, no loss of control was observed at this proximity; our analysis indicates that the strong external alignment torque dominates over local dipole-dipole interactions, ensuring that each nanowire maintains an independent trajectory without interference from the electric fields of its neighbors. Further examples of parallel manipulation, including the tracing of a pine tree with two nanowires and the head of a Labubu character with seven nanowires, are provided in the Supplementary Information (Fig. S7). Movie S5 shows these processes of multiple nanowire calligraphy in parallel. Collectively, these demonstrations underscore the key attributes of our OEM strategy: high stability, parallel operation, and full programmability.

Additionally, our hybrid system retains the versatility of its constituent parts, enabling us to replicate manipulation modalities previously demonstrated using either optical or electric fields alone<sup>33–36</sup>. For instance, by operating in a low-power regime where optical scattering forces dominate the gradient force<sup>33</sup>, we can induce planar translation and rotation of nanowires, as shown in Fig. S8. Moreover, by momentarily increasing the optical power, nanowires can be pushed against the substrate, where they adhere via van der Waals or capillary forces, a technique useful for controlled deposition (Fig. S9). This demonstrates that our OEM platform not only introduces significant performance enhancements but also preserves the rich versatility inherent to optical and electric field manipulation techniques.

To investigate the broader applicability of our OEM strategy, we extended our study to other high-aspect-ratio

biological microstructures, specifically rod-shaped bacteria. These microorganisms often have dimensions comparable to the nanowires studied, making them suitable candidates for testing the versatility of our technique. While optical sorting of bacteria such as *Escherichia coli* has been previously demonstrated<sup>37</sup>, stable trapping and dexterous manipulation of individual rod-shaped bacteria remain challenging. Figure 5a provides a schematic of the proposed manipulation mechanism for rod-shaped bacteria, analogous to that for nanowires. Initially, the bacteria are randomly oriented in suspension. Upon application of the AC field, they undergo dielectrophoretic alignment, which facilitates their subsequent stable trapping and manipulation by the OT. For our experiments, we selected two common probiotic species as model organisms. *Bacillus licheniformis* is a gram-positive thermophilic bacterium commonly found in soil, known for its remarkable adaptability to harsh environmental conditions<sup>38</sup>. *Bifidobacteria*, a genus of gram-positive anaerobes, are microorganisms present in the human body, with some strains used as probiotics<sup>39</sup>. Optical microscope and SEM images of these two bacteria are shown in Fig. 5b, c, respectively. Both species were sourced from commercial medical-grade capsules and prepared for experiments as detailed in the Methods section. The successful application of the OEM strategy is demonstrated in Fig. 5d, which shows a temporal sequence of a *Bacillus licheniformis* bacterium being trapped and maneuvered. An initially free-floating bacterium (highlighted by the white dotted circle) is first shown in a random orientation. Upon activating the electric field, it rapidly aligns with the field direction. The aligned bacterium is then easily captured by the optical trap and translated along a desired path. The entire process is shown in Movie S6. This successful demonstration with biological specimens underscores the general applicability of our hybrid manipulation strategy, indicating its potential for a wide range of applications involving both abiotic and living high-aspect-ratio microstructures.

## Discussion

The discussion first addresses the fundamental mechanism governing the orientation of nanowires in an AC electric field. The observed alignment is driven by a polarization-induced torque. When subjected to an AC electric field, a nanowire develops an induced dipole moment, the nature of which depends on the material. In metallic nanowires, this dipole arises from the redistribution of free charges, while in semiconductor nanowires, it results primarily from the displacement polarization of bound charges.

The interaction of this induced dipole moment with the external field generates a torque that acts to align the

particle's axis of highest polarizability with the field lines. For a prolate spheroid model approximating a nanowire, the time-averaged magnitude of this alignment torque, can be expressed as a function of the angle  $\theta$  between the nanowire's long axis and the electric field<sup>22</sup>:

$$\langle \tau \rangle = \frac{2}{3} \pi a b^2 \epsilon_m (A_S - A_L) \text{Re}[K_L K_S] E^2 \sin 2\theta \quad (1)$$

Here,  $a$  and  $b$  correspond to the semi-axis lengths along the long and short directions;  $\epsilon_m$  is the surrounding medium's permittivity,  $E$  signifies the electric field magnitude, and  $K$  stands for the CM factor,  $A_S$  and  $A_L$  are depolarization factors for short axis and long axis respectively. The full formula can be found in the Supplementary Note: Theory of nanowires in electric field.

This equation shows that the torque is zero at both  $\theta = 0^\circ$  and  $\theta = 90^\circ$ . As quantified by our simulations (Fig. 2j), the torque is restorative, driving the nanowire from the unstable equilibrium at  $\theta = 0^\circ$  toward the stable equilibrium at  $\theta = 90^\circ$ . This theoretical result precisely matches our simulation of the alignment process (Fig. 2a–c) and our experimental observations (Fig. 1e–g). The material-dependent frequency response observed in Fig. 3a–d stems from the different physical origins of the induced polarization, which are well-described by the CM factor and associated interfacial relaxation mechanisms. This frequency behavior is not dictated by the intrinsic plasma frequency of the metal (which is in the optical/UV range), but rather by interfacial charge relaxation (specifically, Maxwell-Wagner relaxation) at the nanowire-medium interface. For metallic nanowires (Ag) in an aqueous medium, the polarization involves both free electrons within the metal and mobile ions in the surrounding fluid. At very low frequencies, mobile ions in the liquid have sufficient time to migrate and form an electric double layer (EDL) at the nanowire surface. This EDL effectively screens the external field, reducing the polarization of the nanowire, which in turn diminishes the induced dipole moment and alignment torque. Consequently, employing a DC electric field is not feasible for this system. A DC field would not only lead to rapid electrolysis of the aqueous medium, generating disruptive bubbles, but would also result in complete screening of the electric field by the double layer, thereby nullifying the alignment torque required for stable trapping. As the frequency increases into the MHz range (as seen in Fig. 3a), the field oscillates too rapidly for the relatively slow-moving ions to form this screening EDL. The screening effect is bypassed, allowing the external field to fully polarize the highly mobile free electrons within the nanowire. This results in a large induced dipole moment and a strong alignment torque. The optimal response

observed at  $\geq 1$  MHz is therefore consistent with this Maxwell-Wagner relaxation, representing the frequency range where ion screening is minimized while the internal electron response remains robust.

Conversely, for semiconductor (GaAs, InAs) and dielectric (TiO<sub>2</sub>) nanowires, the polarization is dominated by their intrinsic dielectric properties (bound charge displacement) and the motion of their internal (and less mobile) charge carriers, rather than the high-density free electrons in a metal. These materials possess different characteristic relaxation frequencies. The optimal mid-frequency range (500 kHz–5 MHz) observed for the semiconductor nanowires likely represents the peak of their specific CM factor, where their polarization relative to the medium is maximized, leading to the strongest alignment torque<sup>40</sup>.

From the perspective of the balance between orientational energy and torque, the torque experienced by the nanowires in an electric field governs their orientation<sup>40,41</sup>.

$$T = \mathbf{p} \times \mathbf{E} = |\mathbf{p}| |\mathbf{E}| \sin \theta \hat{n} \quad (2)$$

$\theta$  is the angle between the long axis and the electric field,  $\mathbf{p}$  is the equivalent electric dipole moment formed by the polarization of the nanowire in the electric field, which characterizes the degree of separation of positive and negative charges.

Due to the high aspect ratio of the nanowire, its polarizability is highly anisotropic. The induced dipole moment is thus described by

$$\mathbf{p} = \boldsymbol{\alpha} \cdot \mathbf{E} \quad (3)$$

where the polarizability tensor  $\boldsymbol{\alpha}$  exhibits a dominant longitudinal component ( $\alpha_{||}$ ) over the transverse component ( $\alpha_{\perp}$ ) due to its high aspect ratio (See the Supplementary Note: Theory of nanowires in electric field for a detailed explanation).

Thus, when the long axis is aligned with the electric field, the nanowires will achieve a maximum dipole moment<sup>42</sup>. The potential energy minimization condition of the system is given by<sup>43</sup>:

$$U = -\mathbf{p} \cdot \mathbf{E} = -|\mathbf{p}| |\mathbf{E}| \cos \theta \quad (4)$$

When  $\theta = 0$  the potential energy is the minimized, the electric field is perfectly aligned corresponding to the long axis.

Furthermore, the magnitude of this alignment torque is intrinsically linked to the geometric anisotropy of the nanowire. In our experiments, we confirmed robust controllability for nanowires with aspect ratios ranging from 5 to 50. Theoretically, as the aspect ratio approaches

1 (spherical geometry), the polarizability anisotropy vanishes, rendering the alignment torque negligible. Our theoretical analysis suggests an effective lower limit of approximately 3, below which the electric alignment torque is insufficient to overcome Brownian rotational diffusion under safe operating voltages.

The second key aspect of our discussion is why the OEM strategy so effectively enhances optical trapping efficiency and stability. This can be understood by analyzing the interplay between optical scattering and gradient forces. In optical trapping, the restorative gradient force is responsible for stable confinement, while the non-conservative scattering force tends to destabilize the trap<sup>44</sup>. For high-aspect-ratio objects like nanowires, the latter often dominates, making stable trapping difficult. The scattering force is proportional to the incident optical power and the particle's scattering cross-section:

$$F_{\text{scat}} = \frac{nP}{c} \sigma_{\text{scat}} \quad (5)$$

With  $n$  the refractive index of the medium,  $P$  the incident optical power,  $c$  the speed of light in a vacuum,  $\sigma_{\text{scat}}$  the scattering cross-section of nanowires.

Our OEM strategy fundamentally alters the balance of these forces. By pre-aligning the nanowire's long axis to be parallel with the beam's propagation direction, the scattering cross-section presented to the incident light is minimized. As confirmed by our simulations, this parallel orientation (Fig. 2f, k) results in a minimal scattering force, whereas the perpendicular orientation (Fig. 2d, k) maximizes it.

When the long axis of the nanowire is aligned with the direction of light propagation, the scattering force acts along the nanowire's long axis (Fig. 1d). In this case, the scattering force is aligned with the direction of motion (axial) of the nanowire, allowing it to overcome viscous resistance. In parallel directions, the strong transverse gradient force cancels out the axial component of the scattered force. In experiments, a lateral gradient force of up to  $10^{-10}$  N can be generated by focusing a Gaussian beam, well exceeding the scattering force ( $10^{-11}$  N).

With the destabilizing scattering force minimized, the gradient force can effectively confine the nanowire. In classical OT theory, the gradient force formula can be expressed as<sup>45</sup>:

$$F_{\text{grad}} = \frac{1}{2} \text{Re}(\alpha) \nabla |E|^2 \quad (6)$$

For a tightly focused beam, the intensity gradient is strongest in the transverse plane. When the nanowire is aligned axially (along the z-axis), it is symmetrically positioned within this strong transverse gradient, which

provides a robust restoring force against any lateral displacements. This optimized transverse confinement, coupled with the drastically reduced axial scattering force, is the primary reason for the observed improvements in trapping success rate and manipulation stability. Furthermore, the stability of this optical trap is directly dependent on the parameters of the applied electric field. The magnitude of the alignment torque (Eq. 1) is proportional to the square of the electric field amplitude. A higher field amplitude thus provides a stiffer rotational confinement, more effectively countering Brownian motion and ensuring the nanowire remains in the optimal, low-scattering-force alignment. This directly translates to a more stable optical trap, capable of sustaining higher manipulation speeds (as shown in Fig. 3g). Similarly, the field frequency is critical. As discussed, the alignment torque is maximized when operating at the optimal frequency range for the material's CM factor (Fig. 3a-d). Operating at non-optimal frequencies would result in a weaker alignment torque, allowing for transient angular fluctuations that increase scattering and decrease trap stability, thereby diminishing the performance gains of the OEM method. It is also worth noting that the vertical alignment induced by the OEM strategy introduces a trade-off between the spatial capturing range and the trapping stability. As characterized in near-field trapping studies<sup>46</sup>, the capturing range represents the spatial domain where the trapping probability exceeds a specific threshold. Theoretically, the reduced geometric cross-section of a vertically aligned nanowire with the Gaussian beam results in a slightly smaller effective interaction volume compared to a randomly oriented (horizontal) nanowire. Our additional experimental observations (details in Fig. S10) confirm a minor reduction in the lateral capture radius. However, this geometric constraint is outweighed by the significant suppression of the axial scattering force. Once the nanowire enters this reduced capture volume, the dominance of the transverse gradient force ensures a substantially stiffer and more robust trap. Consequently, the OEM system trades a marginal decrease in long-range capture capability for a significant improvement in positioning resolution and retention stability, a trade-off that is highly favorable for high-precision nanomanufacturing tasks.

Notably, for metallic nanowires, this parallel alignment may offer an additional benefit by enhancing the efficiency of surface plasmon resonance (SPR) excitation<sup>47,48</sup>. The increased interaction length along the nanowire and suppressed scattering could lead to more efficient coupling of light into plasmonic modes, a subject for future investigation.

Beyond the manipulation of inorganic nanostructures, the biological implications of the OEM strategy are profound, particularly regarding biocompatibility. A critical

limitation of conventional optical tweezers in biological applications is the requirement for high-intensity laser beams, which often induce phototoxicity and detrimental thermal effects that can compromise the viability of living specimens. By introducing the electro-aligning torque, our OEM strategy significantly reduces the optical power threshold required for stable trapping to approximately 7 mW, a 50% reduction compared to conventional methods. This low-power operation capability is pivotal for live-cell manipulation. It drastically minimizes the photon-induced damage and local heating, thereby preserving the physiological integrity and proliferative capacity of sensitive microorganisms, such as the *Bacillus licheniformis* and *Bifidobacterium* demonstrated in this work. Consequently, the OEM platform offers a gentler, more biocompatible approach for cell assembly and analysis, distinguishing it from traditional high-power optical manipulation techniques.

It is instructive to distinguish the proposed OEM strategy from established OET<sup>49,50</sup>. OET relies on photoconductive substrates to generate virtual electrodes, limiting manipulation to a quasi-2D plane near the surface. A major bottleneck of such surface-based techniques is the strong interfacial adhesion (e.g., van der Waals and capillary forces), which often causes nanostructures to irreversibly stick to the substrate. While adding surfactants to the suspension medium is a common strategy to mitigate this stiction, chemical additives can alter surface chemistry or compromise the biocompatibility of sensitive biological samples. In contrast, the OEM strategy utilizes a uniform bulk electric field combined with holographic optical traps, enabling true 3D manipulation of nanowires levitated deep within the fluid chamber (typically > 20  $\mu\text{m}$  from the substrate). By physically separating the nanowires from the boundary, our approach inherently eliminates interfacial stiction without requiring any surfactants, ensuring a pristine chemical environment for complex assembly tasks.

## Conclusion

In summary, this work reports a highly effective OEM strategy that overcomes fundamental limitations in the optical manipulation of high-aspect-ratio nanostructures. Our method synergistically combines a holographic OT system with an AC electric field to achieve unprecedented control. Through detailed theoretical modeling and finite element simulations, we elucidated the underlying physics of the process, quantifying the dielectrophoretic torque responsible for nanowire alignment and modeling the resulting optimization of optical forces. Experimentally, we demonstrated that this electric-alignment strategy effectively constrains the orientation of various metallic and semiconductor nanowires (Ag,  $\text{TiO}_2$ , GaAs, and InAs), preparing them in an optimal configuration for

stable optical trapping. This pre-alignment minimizes the destabilizing optical scattering forces while maximizing the efficacy of transverse gradient forces for confinement. This optimized force balance resulted in substantial performance gains: a 38% increase in trapping success rate, a 50% reduction in the required laser power, and a 39% increase in maximum manipulation speed. The robustness, precision, and scalability of our technique were showcased through advanced manipulation feats, including high-fidelity “nano-calligraphy” and the simultaneous, parallel control of multiple nanowires to assemble complex, pre-programmed patterns. Furthermore, we confirmed the broad applicability and biocompatibility of the OEM strategy by successfully extending it from inorganic nanowires to biological specimens, demonstrating the stable trapping and manipulation of individual rod-shaped bacteria. By integrating multi-physics control with high-resolution optical manipulation, our work establishes a versatile and powerful platform applicable to both abiotic and living materials. This powerful manipulation toolkit opens new avenues for research and technology development, with potential applications in the bottom-up assembly of nanophotonic circuits and scalable quantum devices<sup>51,52</sup>, the construction of photonic neuromorphic networks<sup>53,54</sup>, the development of advanced cellular nanoprobes for biological investigations<sup>55–57</sup>.

## Methods

### Experimental Setup

The experimental configuration is illustrated in Fig. S1. The holographic optical trapping system (SLM-HOT module) was supplied by Shenzhen Kayja-Optics Technology Co. Ltd. and integrated with a modified Nikon ECLIPSE Ti2 inverted microscope. The OT chip consists of two parallel ITO-coated glass substrates (75 mm  $\times$  25 mm  $\times$  0.3 mm, GULUO GLASS), assembled to form a sealed microfluidic chamber containing the liquid medium. Electrical signals were generated using a Keysight 33500B function generator, producing sinusoidal waveforms (1–10<sup>4</sup> kHz, 1 Vpp) amplified to 10 Vpp by an FPA2100 amplifier. A custom-designed chip fixture interfaces the microchamber with the amplifier (Fig. S1). Optical trap generation was controlled via proprietary software on a Lenovo ThinkStation P720 workstation.

### Samples Preparation

Four types of nanowires were used in the experiment. Titanium dioxide (Product number: 774510) and silver nanowires (Product number: 739421) were purchased commercially from Sigma-Aldrich®. Gallium arsenide and indium arsenide nanowires were fabricated, with the detailed manufacturing process provided in the Supplementary Information. All nanowires were dispersed using ultrasonic shaking. Two rod-shaped bacteria, *Bacillus*

licheniformis and *Bifidobacterium*, were purchased from medical-grade live capsules. Before use, a small amount of the powder from the capsule was removed, dissolved in water, and mixed by shaking several times to ensure complete dissolution.

### Numerical Simulations

Finite element models were constructed using COMSOL Multiphysics version 6.2. The Electric Current module was employed to simulate the steady-state electric field characteristics of the nanowires. The Electromagnetic Wave Frequency Domain module was employed to simulate the steady-state optical field characteristics of the nanowires. The specific parameters and theoretical basis of the simulation are provided in the supplementary information.

### Trapping Success Rate

$$R_{\text{success}} = (N_{\text{stable}}/N_{\text{total}}) \times 100\% \quad (7)$$

A successful trap is defined as the nanowire remaining stably confined in the optical trap for at least 5 seconds while being translated at a speed of 5  $\mu\text{m/s}$ . We conducted 10 independent attempts ( $N = 10$ ) for each experimental condition to obtain these statistics.

### Programmable control of the optical trap path

The affine transformation is carried out by means of optical trap position calibration, and the position correspondence between the actual sample plane and the camera image is established, and the relationship between the input coordinates of the phase recovery algorithm used by the spatial optical modulator and the position of the holographic optical trap in the camera screen is established. When path planning is required, the user first sets the actual trajectory and speed of the optical trap based on the position on the camera screen. Once the path planning is initiated, the holographic optical trap is moved according to the settings by updating the phase map projected on the spatial light modulator.

### Acknowledgements

The research was supported by the National Key R&D Program of China (Grants 2024YFC3406900, 2023YFE0112400, 2023YFF0721500, and 2022YFA1207100), the National Natural Science Foundation of China (Grants 62574023, 62575026, 22574015 and 62305023), the Young Elite Scientists Sponsorship Program of CAST (Grant 2023QNRC001), the Beijing Municipal Natural Science Foundation (Grants L254083, L246030, 4242060, and 2242018), Chongqing Municipal Natural Science Foundation (Grant Nos. 2024NSCQ-MSX3784, 2024NSCQ-KJFZMSX0261, CSTB2024NSCQ-JQX0034), Shenzhen Science and Technology Program (Grant No. KJZD20240903101359020), National Key Laboratory of Infrared Detection Technologies (Grant No. IRDT-23-03), Open Research Fund of State Key Laboratory of Digital Medical Engineering (Southeast University, Grant 2025-K07), and the State Key Laboratory of Optoelectronic Materials and Technologies (Sun Yat-sen University, Grant OEMT-2024-KF-03). The authors acknowledge the technical support from the Biological and Medical Engineering Laboratory Center of Beijing Institute of Technology. The

authors also thank Dr. Maoguo Luo (Beijing Institute of Technology, China) for providing technical support in the bacterial samples preparation.

### Author details

<sup>1</sup>School of Mechatronics Engineering, Beijing Institute of Technology, Beijing, China. <sup>2</sup>Zhengzhou Research Institute, Beijing Institute of Technology, Zhengzhou, China. <sup>3</sup>School of Medical Technology, Beijing Institute of Technology, Beijing, China. <sup>4</sup>Chongqing Institute of Microelectronics and Microsystems, Beijing Institute of Technology, Chongqing, China. <sup>5</sup>Engineering Research Center of Integrated Acousto-opto-electronic Microsystems, Beijing, China. <sup>6</sup>School of Integrated Circuits and Electronics, Beijing Institute of Technology, Beijing, China. <sup>7</sup>National Key Laboratory of Infrared Detection Technologies, School of Optics and Photonics, Beijing Institute of Technology, Beijing, China. <sup>8</sup>School of Optics and Photonics, Beijing Institute of Technology, Beijing, China. <sup>9</sup>State Key Laboratory of Semiconductor Physics and Chip Technologies, Institute of Semiconductors, Chinese Academy of Sciences, Beijing, China. <sup>10</sup>Institute of Chemistry, Chinese Academy of Sciences, Beijing, China. <sup>11</sup>Shenzhen Kayja-Optics Technology Co. Ltd., Shenzhen, China. <sup>12</sup>State Key Laboratory of Optoelectronic Materials and Technologies, Sun Yat-sen University, Guangzhou, China

### Author contributions

S.Z. conceived the idea. H.B.L., R.F., B.C., K.L., and Y.Z. designed, fabricated, and characterized the platform. Z.Y.L., C.X., D.P., designed, fabricated, and characterized the nanowires. H.B.L., Z.G., M.Z., and Z.H.L. built the simulation model and ran the simulations. H.B.L., R.F., Z.Y.L., and C.X. carried out the experiments and analyzed the data. H.B.L., H.L., K.C., and R.F. contribute to bacteria experiments. H.B.L., R.F., S.Z., H.X., and J.L. prepared the figures and wrote the manuscript. All authors discussed the results and commented on the manuscript. R.F., Y.Z., Y.C., H.X., J.L., and S.Z. coordinated and supervised the project.

### Data availability

All data needed to evaluate the conclusions in the paper are present in the paper and/or the Supplementary Information.

### Conflict of interest

S.Z., H.B.L., M.Z., R.F., H.L. and Z.G. granted a Chinese patent on technologies related to methodology reported in this work (ZL 202411475226.7). S.Z., H.B.L., R.F., Z.G. and H.L. submitted a Chinese patent on technologies related to methodology reported in this work (CN 202411006659.8).

### Ethics approval and consent to participate

Not applicable.

**Supplementary information** The online version contains supplementary material available at <https://doi.org/10.1038/s41378-026-01225-0>.

Received: 20 November 2025 Revised: 6 January 2026 Accepted: 2 February 2026

Published online: 08 April 2026

### References

- Tian, S., Chen, X. & Ding, B. Manipulation of single nanowire and its applications. *Small Methods* **9**, 2402053 (2025).
- Qin, J., Wu, X., Krueger, A. & Hecht, B. Light-driven plasmonic microrobot for nanoparticle manipulation. *Nat. Commun.* **16**, 2570 (2025).
- Linghu, S. et al. Plasmon-driven nanowire actuators for on-chip manipulation. *Nat. Commun.* **12**, 385 (2021).
- Münning, F. et al. Quantum confinement of the Dirac surface states in topological-insulator nanowires. *Nat. Commun.* **12**, 1038 (2021).
- Zhang, J. et al. Room-temperature ferroelectric, piezoelectric and resistive switching behaviors of single-element Te nanowires. *Nat. Commun.* **15**, 7648 (2024).
- Crane, M. J., Pandres, E. P., Davis, E. J., Holmberg, V. C. & Pauzauskie, P. J. Optically oriented attachment of nanoscale metal-semiconductor heterostructures in organic solvents via photonic nanosoldering. *Nat. Commun.* **10**, 4942 (2019).

7. Ashkin, A., Dziedzic, J. M. & Yamane, T. Optical trapping and manipulation of single cells using infrared laser beams. *Nature* **330**, 769–771 (1987).
8. Ashkin, A. & Dziedzic, J. M. Optical trapping and manipulation of viruses and bacteria. *Science* **235**, 1517–1520 (1987).
9. Chen, J. et al. CRISPR-powered optothermal nanotweezers: diverse bio-nanoparticle manipulation and single nucleotide identification. *Light Sci. Appl.* **12**, 273 (2023).
10. Xiong, J. et al. Photonic nanojet-regulated soft microalga-robot with controllable deformation and navigation capability. *Photonix* **5**, 43 (2024).
11. Yan, Z. et al. Controlling the position and orientation of single silver nanowires on a surface using structured optical fields. *ACS Nano* **6**, 8144–8155 (2012).
12. Yan, Z. et al. Three-dimensional optical trapping and manipulation of single silver nanowires. *Nano Lett.* **12**, 5155–5161 (2012).
13. Zhang, Y. Q. et al. Plasmonic hybridization induced trapping and manipulation of a single Au nanowire on a metallic surface. *Nano Lett.* **14**, 6430–6436 (2014).
14. Wu, Y.-J. et al. Time-varying 3D optical torque via a single beam. *Nat. Commun.* **16**, 593 (2025).
15. Peng, Y. et al. Optothermal ice–water interface management for cross-scale enrichment and molecular sensing. *ACS Nano* **19**, 39281–39291 (2025).
16. Chen, J. et al. Highly-adaptable optothermal nanotweezers for trapping, sorting, and assembling across diverse nanoparticles. *Adv. Mater.* **36**, 2309143 (2024).
17. Lin, L. et al. Opto-thermoelectric nanotweezers. *Nat. Photonics* **12**, 195–201 (2018).
18. Jamshidi, A. et al. Dynamic manipulation and separation of individual semi-conducting and metallic nanowires. *Nat. Photonics* **2**, 86–89 (2008).
19. Yao, J., Yan, H. & Lieber, C. M. A nanoscale combing technique for the large-scale assembly of highly aligned nanowires. *Nat. Nanotechnol.* **8**, 329–335 (2013).
20. Lee, J. et al. Plasmonic biosensor enabled by resonant quantum tunnelling. *Nature Photonics* (2025).
21. Cai, P., Leow, W. R., Wang, X., Wu, Y.-L. & Chen, X. Programmable Nano-Bio Interfaces for Functional Biointegrated Devices. *Adv. Mater.* **29**, 1605529 (2017).
22. Ahmed, W., Kooij, E. S., van Silfhout, A. & Poelsema, B. Quantitative analysis of gold nanorod alignment after electric field-assisted deposition. *Nano Lett.* **9**, 3786–3794 (2009).
23. Li, H. et al. Electric field-induced alignment of Ag/Au nanowires for ultra-sensitive in situ detection of Interleukin-6. *Biosens. Bioelectron.* **271**, 117033 (2025).
24. Arenas-Guerrero, P., Delgado, ÁV., Ahualli, S. & Jiménez, M. L. Polymer-induced orientation of nanowires under electric fields. *J. Colloid Interface Sci.* **591**, 58–66 (2021).
25. Smith, P. A. et al. Electric-field assisted assembly and alignment of metallic nanowires. *Appl. Phys. Lett.* **77**, 1399–1401 (2000).
26. Zhou, R. et al. CdSe nanowires with illumination-enhanced conductivity: induced dipoles, dielectrophoretic assembly, and field-sensitive emission. *J. Appl. Phys.* **101** (2007).
27. Venkatesh, R. et al. Directed assembly of ultrathin gold nanowires over large area by dielectrophoresis. *Langmuir* **31**, 9246–9252 (2015).
28. Fan, D. L., Zhu, F. Q., Cammarata, R. C. & Chien, C. L. Manipulation of nanowires in suspension by ac electric fields. *Appl. Phys. Lett.* **85**, 4175–4177 (2004).
29. Ohta, A. T., Neale, S. L., Hsan-Yin, H., Valley, J. K. & Wu, M. C. in 2008 IEEE/LEOS International Conference on Optical MEMs and Nanophotonics 7-8 (2008).
30. Liu, Y., Chung, J.-H., Liu, W. K. & Ruoff, R. S. Dielectrophoretic assembly of nanowires. *J. Phys. Chem. B* **110**, 14098–14106 (2006).
31. Seo, H. W., Han, C.-S., Hwang, S. O. & Park, J. Dielectrophoretic assembly and characterization of individually suspended Ag, GaN, SnO<sub>2</sub> and Ga<sub>2</sub>O<sub>3</sub> nanowires. *Nanotechnology* **17**, 3388 (2006).
32. Lin, Y.-H., Ho, K.-S., Yang, C.-T., Wang, J.-H. & Lai, C.-S. A highly flexible platform for nanowire sensor assembly using a combination of optically induced and conventional dielectrophoresis. *Opt. Express* **22**, 13811–13824 (2014).
33. Zhang, W. et al. Manipulation of a single metal nanowire by an unpolarized Gaussian beam. *ACS Appl. Mater. Interfaces* **14**, 29111–29119 (2022).
34. Li, H. et al. Precise electrokinetic position and three-dimensional orientation control of a nanowire bioprobe in solution. *Nat. Nanotechnol.* **18**, 1213–1221 (2023).
35. Pauzaskie, P. J. et al. Optical trapping and integration of semiconductor nanowire assemblies in water. *Nat. Mater.* **5**, 97–101 (2006).
36. Agarwal, R. et al. Manipulation and assembly of nanowires with holographic optical traps. *Opt. Express* **13**, 8906–8912 (2005).
37. Shi, Y. et al. Nanophotonic array-induced dynamic behavior for label-free shape-selective bacteria sieving. *ACS Nano* **13**, 12070–12080 (2019).
38. Ding, J. et al. Modeling and optimization of sporulation by *Bacillus licheniformis* BF-002 based on dynamics and recurrent neural networks. *Bioresour. Technol.* **398**, 130534 (2024).
39. Rezaeizadeh, A., Shahabi, S., Bagheri, M., Nabizadeh, E. & Jazani, N. H. The protective effect of *Lactobacillus* and *Bifidobacterium* as the gut microbiota members against chronic urticaria. *Int. Immunopharmacol.* **59**, 168–173 (2018).
40. Jones, T. B. *Electromechanics of Particles*. (Cambridge University Press, Cambridge; 1995).
41. Shao, L. & Käll, M. Light-driven rotation of plasmonic nanomotors. *Adv. Funct. Mater.* **28**, 1706272 (2018).
42. Johnston, M. B. & Joyce, H. J. Polarization anisotropy in nanowires: fundamental concepts and progress towards terahertz-band polarization devices. *Prog. Quantum Electron.* **85**, 100417 (2022).
43. Jackson, J. D. & Fox, R. F. *Classical electrodynamics*, 3rd ed. *Am. J. Phys.* **67**, 841–842 (1999).
44. Neuman, K. C. & Block, S. M. Optical trapping. *Rev. Sci. Instrum.* **75**, 2787–2809 (2004).
45. Zhang, F., Camarero, P., Haro-González, P., Labrador-Páez, L. & Jaque, D. Optical trapping of optical nanoparticles: fundamentals and applications. *Opto-Electron. Sci.* **2**, 230019 (2023).
46. Zaman, M. A., Padhy, P. & Hesselink, L. Capturing range of a near-field optical trap. *Phys. Rev. A* **96**, 043825 (2017).
47. Ndukaife, J. C. et al. Photothermal heating enabled by plasmonic nanostructures for electrokinetic manipulation and sorting of particles. *ACS Nano* **8**, 9035–9043 (2014).
48. Zaman, M. A. & Hesselink, L. Plasmonic response of nano-C-apertures: polarization dependent field enhancement and circuit model. *Plasmonics* **18**, 155–164 (2023).
49. Zaman, M. A., Wu, M., Ren, W. & Hesselink, L. Impedance matching in optically induced dielectrophoresis: effect of medium conductivity on trapping force. *Appl. Phys. Lett.* **125** (2024).
50. Zaman, M. A., Wu, M., Ren, W. & Hesselink, L. Expanding medium compatibility with lateral-field optoelectronic tweezers. *Appl. Phys. Lett.* **127** (2025).
51. Kanne, T. et al. Double nanowires for hybrid quantum devices. *Adv. Funct. Mater.* **32**, 2107926 (2022).
52. Xia, Z. et al. Modulation of nanowire emitter arrays using micro-LED technology. *ACS Nano* **19**, 15813–15819 (2025).
53. Shen, W. et al. SiC@NiO core-shell nanowire networks-based optoelectronic synapses for neuromorphic computing and visual systems at high temperature. *Small* **20**, 2400458 (2024).
54. Qiu, J. et al. Advancements in nanowire-based devices for neuromorphic computing: a review. *ACS Nano* **18**, 31632–31659 (2024).
55. Shi, J., Sun, C., Liang, E. & Tian, B. Semiconductor nanowire-based cellular and subcellular interfaces. *Adv. Funct. Mater.* **32**, 2107997 (2022).
56. Reynolds, D. E. et al. Vertically aligned nanowires for longitudinal intracellular sampling. *ACS Nano* **19**, 13073–13083 (2025).
57. Zhao, X. et al. In situ single-cell surgery and intracellular organelle manipulation via thermoplasmonics combined optical trapping. *Nano Lett.* **22**, 402–410 (2022).